

Experimental study of damage and fracture of cancellous bone using a digital speckle correlation method

Xuefeng Yao

Peng Wang

Tsinghua University
Department of Engineering Mechanics
Beijing 100084, China
E-mail: yxf@mail.tsinghua.edu.cn

Ruchun Dai

Central South University
Institute of Metabolism and Endocrinology
The Second Xiang-Ya Hospital
Changsha, Hunan, China

Abstract. Cancellous bone is a widespread structure in a creature body, for instance, in the femoral head and spondyle. The damage evolution and crack growth of cattle cancellous bone were studied under three-point-bending load conditions. A series of speckle images with deformation information surrounding the crack tip were recorded, and the full-field displacement distributions were obtained at different loading levels by means of digital speckle correlation method (DSCM). Characterizations of the damage deformation and fracture of cancellous bone were analyzed. These results provide some useful information for studying the fracture behavior of cancellous bone.

© 2008 Society of Photo-Optical Instrumentation Engineers. [DOI: 10.1117/1.2928126]

Keywords: cancellous bone; digital speckle correlation method; fracture; damage and deformation.

Paper 07239R received Jul. 3, 2007; revised manuscript received Dec. 1, 2007; accepted for publication Jan. 11, 2008; published online May 19, 2008.

1 Introduction

Cancellous bone has a cellular structure with biological composites for the femoral head and spondyle. It consists of 3D netting trabecular bones. Due to its complex hierarchical structural style, cancellous bone has some physical and mechanical properties that vary by location. This nonhomogeneous characterization results in complicated deformation behavior.¹⁻³ In fact, both the deformation and fracture of cancellous bone are important physiological subjects in necrosis studies of the femoral head and spinal fractures.

At present, most studies about cancellous bone concentrate on the qualitative analysis of microdamage. Yeh and Keaveny studied the relative biomechanical roles of these damage categories by reevaluating the elastic modulus for trabecular bone after simulated overloads to various strain levels using a generic 3D finite element model.⁴ Wang and Niebur investigated the relationship between microdamage propagation and the loading mode in trabecular bone.⁵ They analyzed important microstructural features such as microcrack density, damage area, and microcrack length. Turner et al. compared a fatigued and a nonfatigued bovine bone sample with respect to failure initiation and propagation, and studied the failure mechanism of trabecular bone on the microlevel, using synchrotron light.⁶ However, there are few references in the literature about the quantitative analysis of deformation and fracture.

Traditional experimental techniques for measuring deformation and strain do not allow the characterization of deformation and fracture quantities at the microstructural level in cancellous bone. The digital speckle correlation method (DSCM) has demonstrated its special merits in the deforma-

tion measurement of materials and structures by being non-contact, full field and real time. DSCM provides the full displacement field by comparing two speckle images before and after deformation of the specimen. Nicoletta et al. measured the local microstructural deformations and strains in cortical bone by comparing images acquired from a specimen at two distinct stress states using digital stereo imaging technology.⁷ Turner et al. presented an approach for real-time imaging of human trabecular bone samples under a compression load by using high-speed photography.⁸ They revealed that whitened trabeculae were strongly damaged by microscopic cracks and mostly failed in delamination. Zhang et al. measured the strain distribution on cartilage and vessel tissues by means of an improved DCSM and time-sequence electric speckle pattern interferometry.⁹ Zaslansky et al. mapped deformations on irregular surfaces and measured strain and Young's modulus on various sizes of wet root dentin samples using electronic speckle pattern-correlation interferometry.¹⁰ Duncan et al. provided parametric and nonparametric data processing schemes for analyzing translating laser speckle data used to investigate the mechanical behavior of biological tissues.¹¹ Yao et al. and Meng et al. studied the basic principle of digital speckle correlation technology and its measurement application to many engineering structures.^{12,13}

In this paper, the DSCM was used to study both the deformation characterization and the fracture behavior of cancellous bone. A series of digital speckle images with deformation information were recorded under different loading levels. The full-field displacement distributions were calculated. Some nonhomogeneous deformation and fracture characteristics were analyzed based on the evolution of the damage and crack growth of the cancellous bone.

Address all correspondence to Xuefeng Yao, Department of Engineering Mechanics, Tsinghua University, Qinghua Yuan, Beijing 100084 China; Tel: 86-10-62771546; Fax: 86-10-62781824; E-mail: yxf@mail.tsinghua.edu.cn

2 Digital Speckle Correlation Method

The DSCM can compare two images of a specimen in a undeformed and deformed states by using image recognition technology. The key of DSCM is to search for the maximum correlation between small zones in the deformed and reference images from which the displacement can be obtained at different positions in the zone of interest. The simplest image-matching procedure is cross correlation, which can determine the in-plane displacement field (u, v) by matching different zones of two images.^{14,15} In this paper, the correlation equation in the DSCM calculation is shown in Eq. (1):

$$C(u, v) = \frac{\sum_{i=1}^m \sum_{j=1}^m [f(x_i, y_j) - \bar{f}][g(x'_i, y'_j) - \bar{g}]}{\sqrt{\sum_{i=1}^m \sum_{j=1}^m [f(x_i, y_j) - \bar{f}]^2} \sqrt{\sum_{i=1}^m \sum_{j=1}^m [g(x'_i, y'_j) - \bar{g}]^2}}, \quad (1)$$

where $f(x, y)$ is the gray-level value at coordinates (x, y) for the original image, $g(x', y')$ is the gray-level value at coordinates (x', y') for the target image, C is the maximum correlation factor, and \bar{f} and \bar{g} are the average gray values of the image $f(x, y)$ and $g(x, y)$, respectively. The coordinates (x, y) and (x', y') are related by the deformation that occurred between the two images. If the motion of the object relative to the camera is parallel to the image plane, the relation between the coordinates (x, y) and (x', y') can be expressed as

$$\begin{cases} x' = x + u + \frac{\partial u}{\partial x} \Delta x + \frac{\partial u}{\partial y} \Delta y \\ y' = y + v + \frac{\partial v}{\partial x} \Delta x + \frac{\partial v}{\partial y} \Delta y, \end{cases} \quad (2)$$

where u and v are the displacement components of the subset centers in the x and y directions, respectively. The terms Δx and Δy are the distances from the subset center to point (x, y) . Digital image correlation technology is used to obtain the six deformation parameters for u , v , $\partial u / \partial x$, $\partial u / \partial y$, $\partial v / \partial x$, and $\partial v / \partial y$.

Based on the peak value and the symmetrical character of the correlation coefficient C as shown in Fig. 1, a cross-search method is used to make the speed of the search about one order of magnitude faster than the traditional approach. First, the displacement in an integer number of pixels (image unit) is extracted by determining the average displacement of the deformed image with respect to the reference image when the maximum of the cross-correlation function is evaluated at each pixel location (x, y) of the zone of interest. Second, a subpixel correction of the displacement is obtained by determining the maximum of a parabolic interpolation of the correlation function. This interpolation is performed by considering the maximum pixel and its eight nearest-neighbor points. After finding the first peakpixel, a quadratic Lagrange interpolation function $C'(x, y)$ of the correlation function is adopted as shown in Eq. (3):

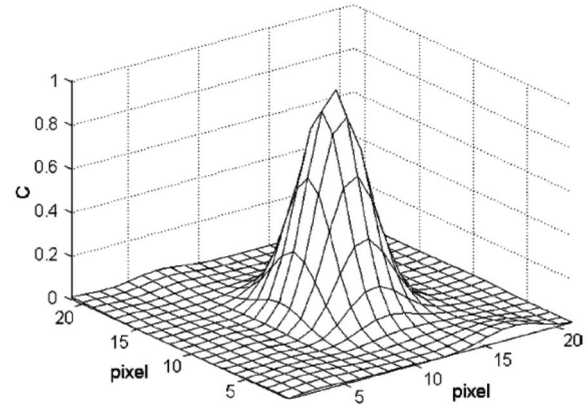


Fig. 1 Peak and symmetrical distribution of correlation coefficients.

$$C'(x, y) = Ax^2y^2 + Bx^2y + Jx^2 + Dxy^2 + Exy + Fx + Gy^2 + Hy + I. \quad (3)$$

Thus, the precise position of the subpixel will be searched. It is obvious that the nine correlation coefficients $(A, B, J, D, E, F, G, H, I)$ of a 3×3 area surrounding this peak point can be determined.^{13,15}

The maximum value can be determined by differentiation of the function $C'(x, y)$:

$$\frac{\partial C'}{\partial x} = \frac{\partial C'}{\partial y} = 0. \quad (4)$$

After using the above processing procedure, the subpixel search becomes much simpler and more precise. This kind of image recognition method results in a much better measurement of the displacement field.

3 Experimental Detail

3.1 Preparation of Cancellous Bone Specimen

In this study 10 fresh cancellous bones were obtained from the femoral heads of five adult cattle. Five fresh cancellous bones were from the left legs of five adult cattle; the other five fresh cancellous bones were from the right legs of the other five adults. Ten rectangular specimens of cancellous bone were cut from 10 fresh cancellous bones using a special medical thin saw with a 0.2-mm-thick diamond blade. The specific locations of the cancellous bone specimens in the femoral head are shown in Fig. 2. Due to the porous structure and brittleness of cancellous bones, it is difficult to make all specimens the same size. The specific sizes (length \times height \times thickness) of the 10 specimens in this study are shown in Table 1. These samples were stored in a 0.9% sodium chloride solution.

Before the formal experiments, an initial crack (1.26-mm length) was made, using the special medical thin saw, in the middle of the longitudinal side of the specimen. The crack was made parallel to the direction of the height side.

3.2 Experimental Information

Figure 3 shows the geometrical configurations and loading conditions of the cancellous bone specimens. A schematic dia-

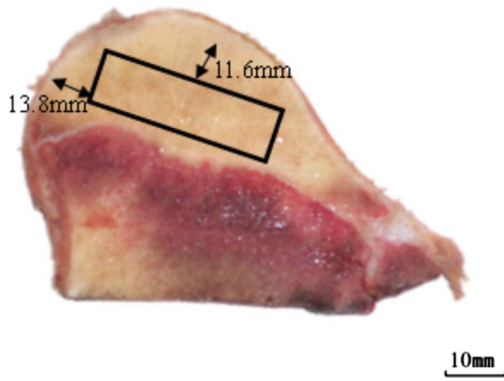


Fig. 2 Location of cancellous bone specimen in the femoral head.

gram of digital speckle correlation technology is shown in Fig. 4

In this experiment, the experimental setup for the digital speckle correlation technology consisted of a special test machine, a charge-coupled-device (CCD) camera, an optical fiber cold light source, and digital image correlation processing software written in C++ language. The test machine was controlled by a computer, the moving velocity of the cross-head was 0.5 mm/min, and the load was measured using a force transducer. The displacement of the load tip was measured by the displacement transducer. In the three-point-bending experiment, the distance between the two supports was 26 mm.

In the DSCM, the specimen surfaces were sprayed with black and white paint to form a random pattern. This pattern was prepared by coating the surface with white paint and then allowing the overspray from a can of black paint to speckle the white surface. It is easy to find the image pairs with this kind of black and white pattern using the digital image correlation method.

In this experiment, the cold light source was the common visible white light, which passes through the optical fiber to illuminate the specimen surface. This cold light source had 380-nm center wavelengths with 30-nm bandwidths, and the corresponding coherence length was 10 mm. The CCD camera was used to record the speckle image of the specimen surface with a resolution of 1280 × 1024 pixels. The image was monochrome, and the brightness was represented by grey levels. Grey level 0 represented the darkest point and grey level 255 was the brightest area. In this experiment, a point with white paint showed the brightest and one with black

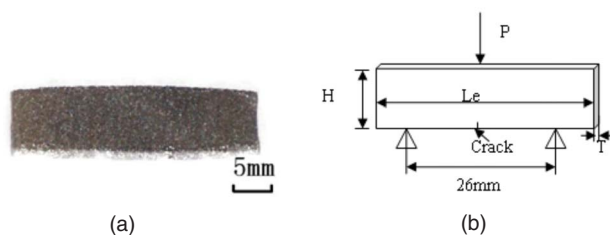


Fig. 3 Three-point-bending test of cancellous bone specimen. (a) Cancellous bone specimen. (b) Geometrical configuration and loading condition.

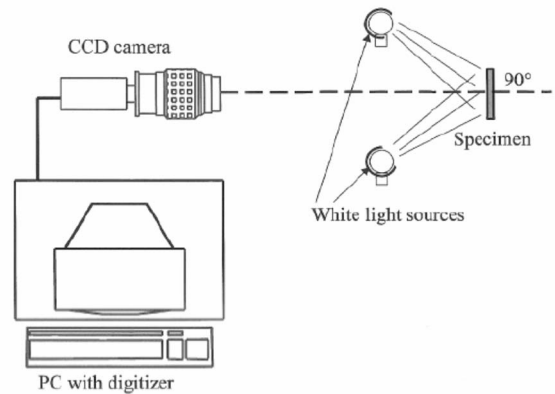


Fig. 4 Schematic diagram of digital speckle correlation technology.

paint was the darkest. The average speckle characteristic size was about 3 pixels, or 0.12 mm (because 25.17 pixels represents 1 mm in this experiment).

4 Experimental Results and Discussions

4.1 Load-Displacement Curves in Cancellous Bone Specimens

Due to the thickness differences in the 10 cancellous bone specimens, the force per unit thickness γ was defined by

$$\gamma = \frac{F}{T}, \quad (5)$$

where F represents the actual applied load, and T is the width of the specimen.

After a series of three-point-bending tests, the relationship between the force per unit thickness and the displacement for the 10 cancellous bone specimens was determined, as shown

Table 1 Specific dimensions of cancellous bone specimens.

No.	Side of leg	Length(Le) (mm)	Thickness(T) (mm)	Height(H) (mm)
1	Left	32.00	2.86	10.00
	Right	31.92	1.98	10.00
2	Left	31.80	1.98	10.90
	Right	31.60	2.34	10.00
3	Left	32.10	2.16	10.34
	Right	31.96	2.10	10.16
4	Left	32.10	2.70	10.40
	Right	32.06	2.26	10.40
5	Left	31.90	2.26	10.14
	Right	32.00	2.30	10.30

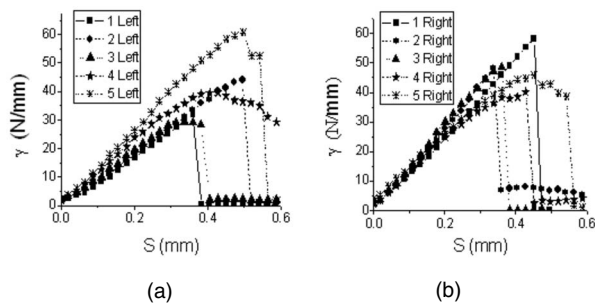


Fig. 5 Relationship between the displacement S and the force per unit thickness γ for cancellous bone specimens: (a) specimens from left femoral head; (b) specimens from right femoral head.

in Fig. 5(a). It is obvious that there is an approximately linear relationship between the load and the displacement before the damage initiation and fracture of the specimen. Some fluctuations in the load-displacement curves resulted from the initiation and progress of microdamage in the trabecular bone. Once the load reached the maximum value, a lot of damage appeared at the crack tip. Then the crack was initiated and began to grow. In the meantime, the loading capacity of the cancellous bone specimen was reduced with the evolution of the damage and the propagation of the crack in the specimen. These fracture phenomena can be attributed to the hierarchical graded structure and the complex mechanical properties of the cancellous bone. In this experiment, the average force per unit thickness was about 44.6 N/mm.

4.2 Speckle Patterns of Damage and Fracture in Cancellous Bone

While the three-point-bending tests of cancellous bone specimens were performed, the deformation fields surrounding the crack tip of the specimens were recorded in the form of speckle patterns using the CCD camera. These images revealed the whole deformation and fracture process of the cancellous bone specimens, including elastic deformation, damage evolution, and crack initiation and propagation. On the whole, the deformation and fracture of cancellous bone can be divided into three patterns: elastic deformation, damage evolution, and crack growth. Figure 6 gives a typical image of deformation and fracture of a cancellous bone specimen for the left leg (no. 5). Here, S represents the displacement, P is the applied load and L represents the crack length.

In the initial loading stage, the deformation of the specimen was considered as the elastic state. While the applied load was increased gradually, the stress concentration at the crack tip will be further buildup. When the applied load reached the maximum value, the damage at the crack tip appeared and evolved. Subsequently, the crack tip was initiated and propagated. During the whole growing process of the crack, the damage at the running crack tip developed successively. Due to the hierarchical graded structure characterization of cancellous bone, the crack locus in the fracture displayed an irregular curve. Also, the roughness of the fracture surface was rather high due to the broken trabecular bone and the tearing of the reseau in cancellous bone.

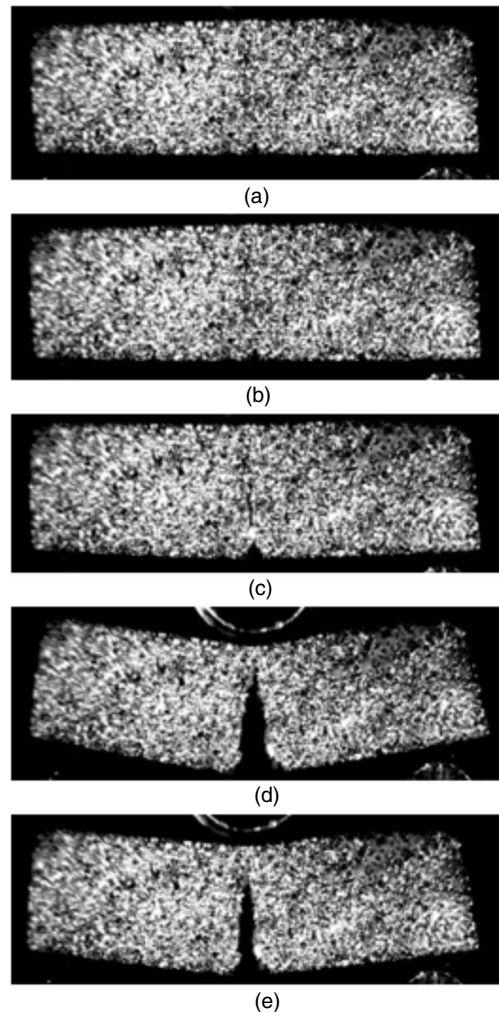


Fig. 6 Typical images on deformation and fracture of cancellous bone specimen for the left leg (no. 5): (a) Elastic deformation ($S = 0.05$ mm, $P = 8$ N, $L = 1.26$ mm); (b) Damage evolution ($S = 0.18$ mm, $P = 49$ N, $L = 1.26$ mm); (c) Damage initiation and crack growth ($S = 1.05$ mm, $P = 2.26$ N; $L = 5.16$ mm); (d) Crack propagation and fracture ($S = 2.00$ mm, $P = 1$ N, $L = 7.79$ mm); (e) Recovery stage.

4.3 Deformation Field of Cancellous Bone

After making digital image correlation calculations from the speckle patterns, we obtained the full-field U and V displacements, where U and V represent the displacement components in the horizontal X and vertical Y directions, respectively. In the DSCM test system, the measurement accuracy of the displacement was 0.05 pixel, or 0.002 mm (because 25.17 pixels represents 1 mm in this experiment).

Figure 7 shows the elastic deformation field of the specimen before the cracking damage appeared, when the load was from 132N to 137N ($\Delta P = 5$ N). The full-field displacement distribution of cancellous bone was almost the same as the typical displacement field in a three-point-bending homogeneous specimen. According to the distribution of maximum correlation factors at every point in Fig. 7(d), the maximum correlation factors at each point were all above 0.91, which means that the full-field displacements U and V in Figs. 7(b) and 7(c) are reliable and acceptable.

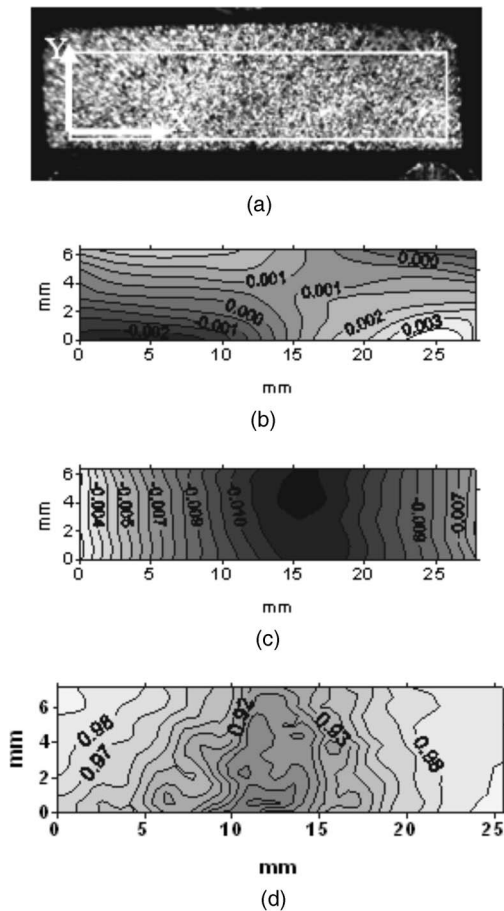


Fig. 7 Displacement field of the specimen in the left leg (no. 5) before the damage evolution when the load was from 132N to 137N ($\Delta P = 5N$): (a) calculation zone; (b) displacement field in the X direction, (c) displacement field in the Y direction; (d) maximum correlation factor.

While the applied load was increased and reached the maximum value, the damage at the crack tip appeared and evolved. The full-field displacement at the static crack tip is shown in Fig. 8. In this period, although the damage zone area ahead of the crack tip increased, the crack tip position was still unchanged, as shown in Fig. 8(a). In other words, the crack was in a stationary state. In Fig. 8(b), an arrow tip points to the damage position at the crack tip. Also, the strain concentration at the crack tip developed because the displacement contours at the crack tip were denser than those at any other positions. The displacement field in the vertical Y direction shows no distinct difference from that in Fig. 7(c). Due to the evolution of damage, the correlation factor of the displacement field calculation was a little lower than the one in Fig. 7(e), but the correlation factor was still above 0.86 and is reliable and acceptable. The reason for this phenomenon is that the speckle image at the crack tip was distorted when the damage evolved.

While the applied load was further increased, the damage at the crack tip evolved and the crack began to propagate. Figure 9 shows the displacement field of the specimen in the left leg (no. 5) during crack propagation. Because the crack tip damage and growth almost reached the top side of the

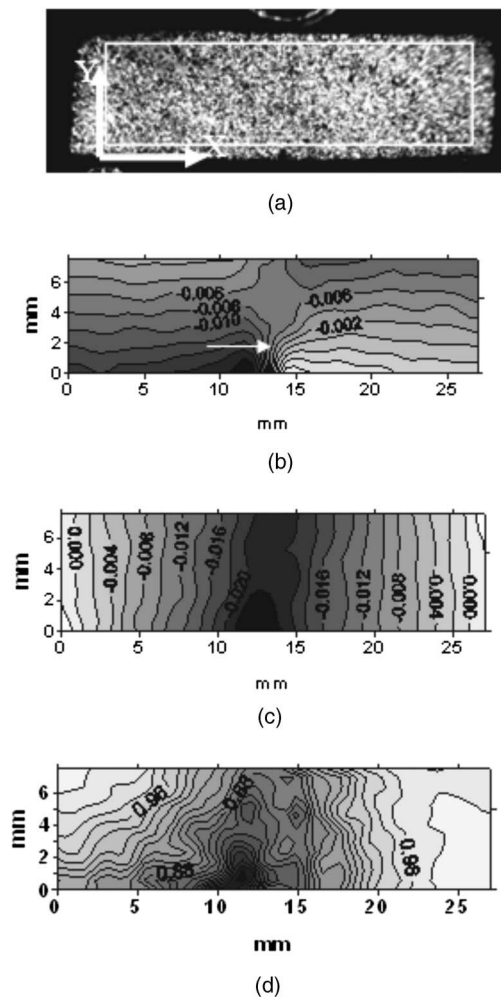


Fig. 8 Displacement field of the specimen in the left leg (no. 5) during the damage evolution when the load was from 123N to 122N ($\Delta P = -1N$): (a) calculation zone; (b) displacement field in the X direction; (c) displacement field in the Y direction; (d) maximum correlation factor.

specimen, the displacement distribution in the X direction is different from those in Figs. 7(b) and 8(b). The displacement field in the Y direction has no distinct difference from those in Figs. 8(c) and 9(c). From the distribution of the maximum correlation factor in Fig. 9(d), the maximum correlation factor at some positions is lower than 0.9. But since it is still higher than 0.85, the related results are reliable and acceptable. Again, the reason for this phenomenon is that the speckle image at the crack tip was distorted when the damage evolved and the crack propagated.

Based on the above stated experimental results, the neutral axis of the specimen in Fig. 7(b) is in the middle of the specimen like in the normal three-point-bending experiment. The neutral axis moved up toward the load tip top side of the specimen in Figs. 8(b) and 9(b) when the damage evolved and the crack propagated.

As shown in Figs. 7(d), 8(d), and 9(d), the correlation factor near the crack was smaller than those at other places. In particular, the speckle correlation factor at the damage zone in the DSCM calculation decreased, as shown in Figs. 8(d) and

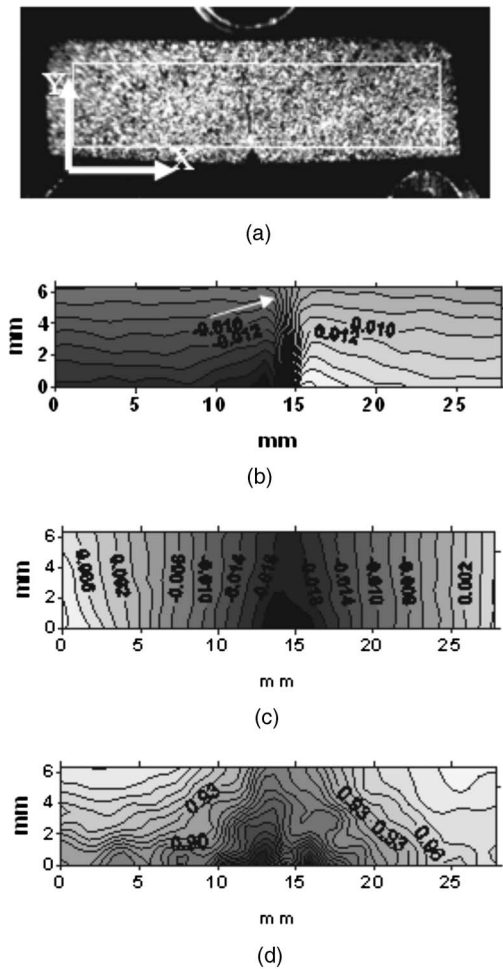


Fig. 9 Full displacement field of the specimen in the left leg (no. 5) during crack propagation when the load was from 2.26N to 2.51N ($\Delta P=0.25N$): (a) calculation zone; (b) displacement field in the X direction; (c) displacement field in the Y direction; (d) maximum correlation factor.

9(d) when the calculated zone was within the damage zone of the specimen. The explanation is that cancellous bone is made of cellular tissue with many trabeculars; both the deformation of the specimen itself and the relatively rigid movement of the trabecular bones were caused simultaneously under the applied load, and the speckle image in the damage zone was distorted due to the structural changes of the cancellous bone. Finally, the speckle correlation coefficient of the DSCM calculation decreased, in addition to the changes in surface configuration of the specimen.

4.4 Damage Length and Crack Length of Cancellous Bone Specimen

During the fracture process of the cancellous bone specimen, both the damage evolutions at the crack tip and the crack propagation were concurrent. Usually the damage at the crack tip happened before the crack initiation and propagation. The propagation of the damage zone and the crack growth terminated at the load tip location near the top side of the specimen. Here Both the damage length and the crack length were

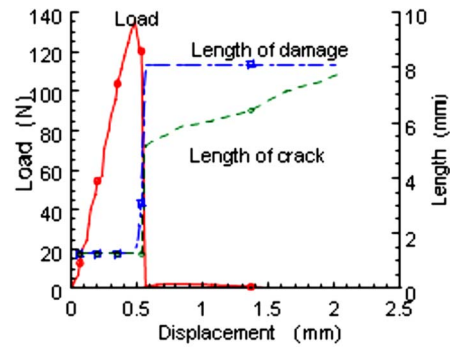


Fig. 10 Relationship among load, crack damage, and displacement of the left leg specimen (no. 5).

used to describe the fracture behavior of the specimen. In the crack tip damage zone, the cancellous bone was still connected and the crack was not initiated.

As a typical example illustration, Fig. 10 shows the corresponding relationships among the load, crack length, damage length, and load-tip displacement in the whole damage and fracture process of the left leg specimen (no. 5). Both the damage length and the crack growth length were obtained by analyzing the image information of the speckle pattern in Fig. 6. The size of the damage zone increased sharply and the crack length increased step by step when the applied load was decreased sharply. Finally, The crack length was the same as the damage zone size. This phenomenon means that it is the size of the damage zone, not the crack length, that determines the loading capacity of the specimen. Thus, the size of the damage zone is important data in studying the fracture of cancellous bone.

5 Conclusion

This paper reported on deformation and fracture behavior of cancellous bone that was experimentally studied using the DSCM. Some important conclusions are summarized as follows:

1. During the process of fracture in the cancellous bone, three kinds of patterns were shown: elastic deformation, damage, and crack growth. In particular, both the crack tip damage and the crack growth were concurrent with the crack propagation. Also, the crack tip damage happened before of the crack initiated and propagated. The crack tip damage determines the loading capacity of cancellous bone.
2. A series of speckle images about the deformation and fracture in the cancellous bone specimen were recorded. The full-field displacement distributions of the cancellous bone were calculated using the DSCM, including elastic deformation, damage deformation, and the displacement field during the crack propagation. The experimental results about the displacement field and the correlation coefficient revealed the potential and reliability of the DSCM technology in the analysis of bone damage evolution.
3. The speckle correlation coefficient of the DSCM calculation in the damage zone at the crack tip decreased compared to the other positions in the specimen. The explanation is that the cancellous bone consists of porous tissue with many trabeculars. Both the deformation of trabecular bone itself and

the relatively rigid movement of trabeculars were caused simultaneously under the applied load. The speckle image in the damage zone was distorted due to the structural changes of the cancellous bone.

Acknowledgments

This research project was supported by the China Nature Science Foundation (No. 30470430 and No. 30400514).

References

1. Y. C. Fung, *Biomechanics—Mechanical Properties of Living Tissues*, 2nd edition, Springer Press, 500–536 (1993).
2. L. J. Gibson, “Biomechanics of cellular solids,” *J. Biomech.* **38**, 377–399 (2005).
3. L. J. Gibson and M. F. Ashby, *Cellular Solids—Structure and Properties*, 2nd edition, Cambridge University Press, 429–452 (1997).
4. O. C. Yeh and T. M. Keaveny, “Relative roles of microdamage and microfracture in the mechanical behavior of trabecular bone,” *J. Orthop. Res.* **19**(6), 1001–1007 (2001).
5. X. A. Wang and G. L. Niebur, “Microdamage propagation in trabecular bone due to changes in loading mode,” *J. Biomech.* **39**(5), 781–790 (2006).
6. P. J. Thurner, P. Wyss, R. Voide, M. Stauber, M. Stampanoni, U. Sennhauser, and R. Muller, “Time-lapsed investigation of three-dimensional failure and damage accumulation in trabecular bone using synchrotron light,” *Bone (N.Y.)* **39**(2), 289–299 (2006).
7. D. P. Nicoletta, A. E. Nicholls, J. Lankford, and D. T. Davy, “Machine vision photogrammetry: a technique for measurement of microstructural strain in cortical bone,” *J. Biomech.* **34**(1), 135–139 (2001).
8. P. J. Thurner, B. Erickson, R. Jungmann, Z. Schriock, J. C. Weaver, G. E. Fantner, G. Schitter, D. E. Morse, and P. K. Hansma, “High-speed photography of compressed human trabecular bone correlates whitening to microscopic damage,” *Eng. Fract. Mech.* **74**(12), 1928–1941 (2007).
9. J. Zhang, G. C. Jin, L. B. Meng, L. H. Jian, A. Y. Wang, S. B. Lu, “Strain and mechanical behavior measurements of soft tissues with digital speckle method,” *J. Biomed. Opt.* **10**(3), 034021 (2005).
10. P. Zaslansky, J. D. Currey, A. A. Friesem, and S. Weiner, “Phase shifting speckle interferometry for determination of strain and Young’s modulus of mineralized biological materials: a study of tooth dentin compression in water,” *J. Biomed. Opt.* **10**(2), 024020 (2005).
11. D. D. Duncan and S. J. Kirkpatrick, “Processing algorithms for tracking speckle shifts in optical elastography of biological tissues,” *J. Biomed. Opt.* **6**(4), 418–426 (2001).
12. X. F. Yao, L. B. Meng, G. C. Jin, and H. Y. Yeh, “Full-field deformation measurement of fiber composite pressure vessel using digital speckle correlation method,” *Polym. Test.* **24**, 245–251 (2005).
13. L. B. Meng, G. C. Jin, and X. F. Yao, “Application of iteration and finite element smoothing technique for displacement and strain measurement of digital speckle correlation,” *Opt. Lasers Eng.* **45**(1), 57–63 (2007).
14. H. A. Bruck, S. R. McNeill, M. A. Sutton, and W. H. Peters III, “Digital image correlation using Newton–Raphson method of partial differential correlation,” *Exp. Mech.* **29**, 261–267 (1989).
15. G. C. Jin, Z. Wu, N. K. Bao, and X. F. Yao, “Digital speckle correlation method with compensation technique for strain field measurements,” *Opt. Lasers Eng.* **39**, 457–464 (2003).